ARL-TR-7835 ● SEP 2016

ARL

US Army Research Laboratory

The Mechanics of a Crack Parallel to a Rigid Boundary Under Remote Tension

by George A Gazonas and Brian M Powers

NOTICES

Disclaimers

The findings in this report are not to be construed as an official Department of the Army position unless so designated by other authorized documents.

Citation of manufacturer's or trade names does not constitute an official endorsement or approval of the use thereof.

Destroy this report when it is no longer needed. Do not return it to the originator.

ARL

US Army Research Laboratory

The Mechanics of a Crack Parallel to a Rigid Boundary Under Remote Tension

by George A Gazonas and Brian M Powers
Weapons and Materials Research Directorate, ARL

REPORT DOCUMENTATION PAGE

1. REPORT DATE *(DD-MM-YYYY)* September 2016	2. REPORT TYPE Technical Report	3. DATES COVERED (From - To) March 2016–August 2016

4. TITLE AND SUBTITLE The Mechanics of a Crack Parallel to a Rigid Boundary Under Remote Tension	5a. CONTRACT NUMBER
	5b. GRANT NUMBER
	5c. PROGRAM ELEMENT NUMBER
6. AUTHOR(S) George A Gazonas and Brian M Powers	5d. PROJECT NUMBER AH84
	5e. TASK NUMBER
	5f. WORK UNIT NUMBER

7. PERFORMING ORGANIZATION NAME(S) AND ADDRESS(ES) US Army Research Laboratory ATTN: RDRL-WMM-B Aberdeen Proving Ground, MD 21005-5066	8. PERFORMING ORGANIZATION REPORT NUMBER ARL-TR-7835

9. SPONSORING/MONITORING AGENCY NAME(S) AND ADDRESS(ES)	10. SPONSOR/MONITOR'S ACRONYM(S)
	11. SPONSOR/MONITOR'S REPORT NUMBER(S)

12. DISTRIBUTION/AVAILABILITY STATEMENT
Approved for public release; distribution is unlimited.

13. SUPPLEMENTARY NOTES
primary author's email: <george.a.gazonas.civ@mail.mil>.

14. ABSTRACT
In this report, we present the method of integral transforms and the Gauss-Chebyshev quadrature methods to solve the problem of a crack parallel to a rigid boundary under remote tension. We derive a system of singular integral equations of the first kind, specific to the problem at hand, which we numerically solve using Gauss-Chebyshev integration. We specialize our results to the problem of a crack in an infinite plate under remote tension, and show that the relative error in our numerically derived solutions are within machine precision of the closed-form analytical solutions. Stress intensity factors are calculated that are in excellent agreement with those derived by others using different methods. We also demonstrate that both the stress intensity factors and normal $\sigma_{yy}(x,y)$ and shear $\sigma_{xy}(x,y)$ stress fields derived via numerical solution of the singular integral equations, compare well with those determined using the commercially available Abaqus finite element code where the crack is modeled using the eXtended Finite Element Method.

15. SUBJECT TERMS stress intensity factors, singular integral equations, Fourier integral transforms, Gauss-Chebyshev integration, Abaqus, XFEM, Mathematica

16. SECURITY CLASSIFICATION OF:			17. LIMITATION OF ABSTRACT	18. NUMBER OF PAGES	19a. NAME OF RESPONSIBLE PERSON George A Gazonas
a. REPORT Unclassified	b. ABSTRACT Unclassified	c. THIS PAGE Unclassified	UU	52	19b. TELEPHONE NUMBER (Include area code) 410-306-0863

Contents

List of Figures

List of Tables

Acknowledgments

The authors wish to thank Dr Tomoko Sano of the US Army Research Laboratory for aid in translating portions of the article by Yokobori et al. (1971).[*]

INTENTIONALLY LEFT BLANK.

1. Introduction

The primary motivation for the current study comes from our recent work[1] on wave propagation in microcracked media under prestress; our interest in this report is to gain an understanding of why compressive stresses of $\sigma_{yy} = -90$ MPa develop between stationary (non-propagating) fractures in a medium under a remote tensile prestress of $\sigma_{yy} = 50$ MPa (cf. Fig. 11(a) in Sahane et al.[1] reproduced in part here in Fig. 1). Because of the stress concentrations at the crack tips, the maximum tensile stress $\sigma_{yy} = 490$ MPa is an order of magnitude higher than the applied tensile far-field prestress, but closely arranged parallel fractures areas of compressive stress (dark blue) can develop that are significant in magnitude relative to the applied tensile prestress.
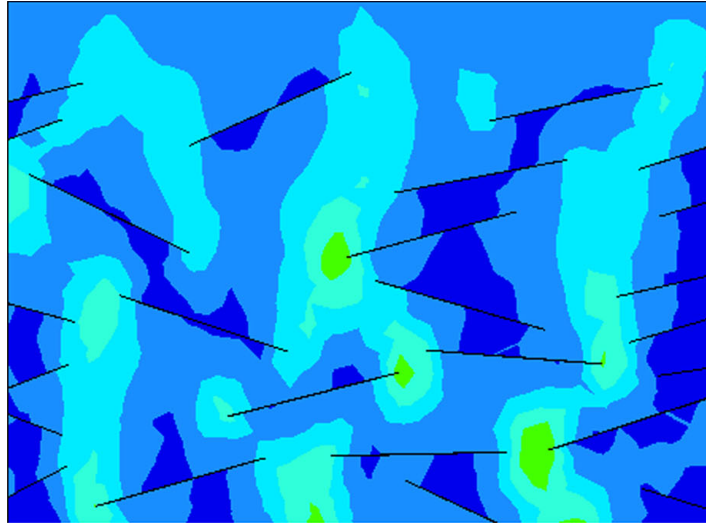
Fig. 1 An Abaqus[2] simulation[1] showing that a fractured medium under a tensile far-field prestress of 50 MPa can generate compressive stresses (dark blue coloration) between fractures in close proximity

The problem of wave propagation in a prestressed medium was originally studied by Biot[3,4] and later applied to problems in geophysics related to self-gravitation of the spherical earth,[5] subsurface detonations,[6] the propagation of Rayleigh[7] and Scholte[8] waves, and borehole diagnostics.[9] Applications that involve prestressed media range from "compliant" materials, (e.g., vascular materials,[10] dielectric polymers[11] and magnetorheologic elastomers[12]), to relatively "brittle" materials, (e.g., concrete,[13] ceramics,[14] and glass[15]).

The complexity of the prestress mechanics problem increases dramatically when one considers the influence of microcracks on wave propagation and other properties, such as electrical properties; such problems can be addressed using the class of homogenization methods known as generalized self-consistent methods (GSCMs).[16–19] GSCMs permit derivation of the anisotropic effective moduli for the medium in cases where the cracks are relatively dilute, i.e., are non-interacting and stationary. The problem in which discrete cracks interact with each other, but are stationary, was addressed by Sahane et al.,[1] and the solution of the more general case where the microcracks both interact and propagate across spatial scales requires the use of concurrent multiscale methods.[20]*

To answer the question posed earlier, in this report, we study the mechanics of the 2 overlapping parallel crack problem under remote tension, and show that this problem is mechanically equivalent to the problem of a single crack parallel to a rigid boundary (shear-stress free symmetry plane) under remote tension (see Fig. 2(c)).

In Section 2, we present the method of integral transforms[21] to solve the problem of a crack parallel to a rigid boundary under remote tension. In Section 3, we apply the methods developed by Erdogan and Gupta[22,23] and develop a system of singular integral equations of the first kind (with a Cauchy-type singularity), which is numerically solved using Gauss-Chebyshev integration. Fortunately, stress intensity factors (SIFs) for this problem are derived using the Schwartz-Neumann alternating technique[24] (or method of successive approximations) by Chang and Ma[25] who provide a table of SIFs which they compare with the earlier work of Yokobori et al.[26] and Kamei and Yokobori.[27] The SIFs we derive in Section 4 of this report are in excellent agreement with the earlier works that use different methods for their derivation.[25–27] In Section 5, we derive expressions for the normal stress $\sigma_{yy}(x, y)$ and shear stress $\sigma_{xy}(x, y)$ fields in the region between the crack and the rigid boundary (symmetry plane) and demonstrate that this region is indeed in a state of compression, as our prior finite element [FE] simulations indicate in Fig. 1, despite the remotely applied tensile prestress. We also demonstrate that both the SIFs and stress fields derived via numerical solution of the singular integral equations, compare well with those determined using the commercially available Abaqus/Standard[2] FE code. Section 6 focuses on estimating the relative error in

our numerically derived solutions by specializing them to the closed-form analytical solutions found in Zehnder;[28] our numerical solutions are found to be within machine precision of the closed-form analytical solutions. In Section 7 we use this result to estimate the relative error between the normal and shear stress distributions using the numerical solution of the singular integral equations and Abaqus FE results. Section 8 outlines the Abaqus FE model geometry and boundary conditions used to solve the boundary value problem; the crack is modeled in Abaqus using the eXtended Finite Element Method (XFEM), which is used to predict FE-based SIFs, which are compared with those determined using our numerical solutions. Conclusions follow in Section 9.

2. Governing Equations

This section outlines the solution method for the crack boundary value problem illustrated in Fig. 2(c), where the crack interval $(-a, +a)$, without loss of generality, can been normalized to $(-1, +1)$. This solution can be obtained by superposition of the solution to the problem of a uniformly pressurized crack shown in Fig. 3(b), with the solution to the problem of a semi-infinite medium, without a crack, but uniformly loaded at infinity $\sigma_{yy} = \sigma_{-\infty} = P_0$ shown in Fig. 3(c).

(a)   (b)   (c)
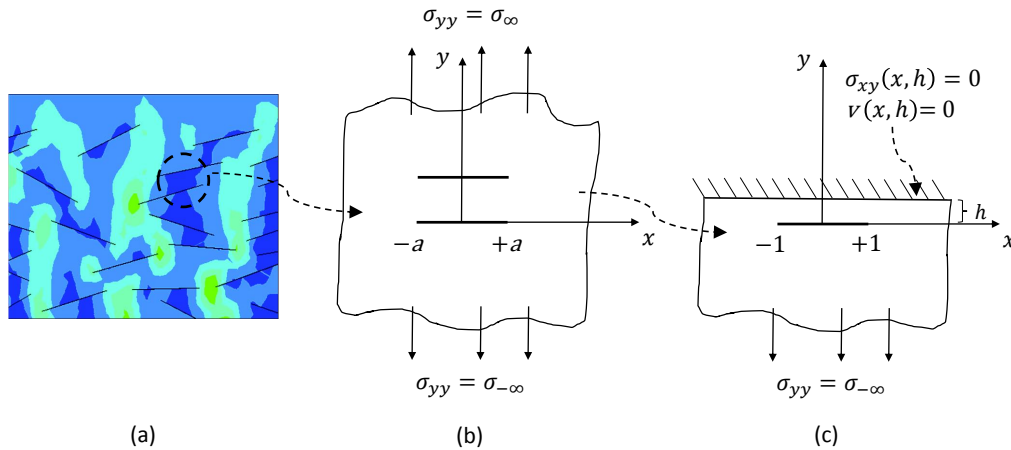
Fig. 2 A fractured medium subjected to a remote tensile load; (a) Abaqus[2] simulation,[1] and the equivalence of the (b) 2 overlapping parallel crack problem with the (c) single crack parallel to a rigid boundary (shear-stress free symmetry plane) problem
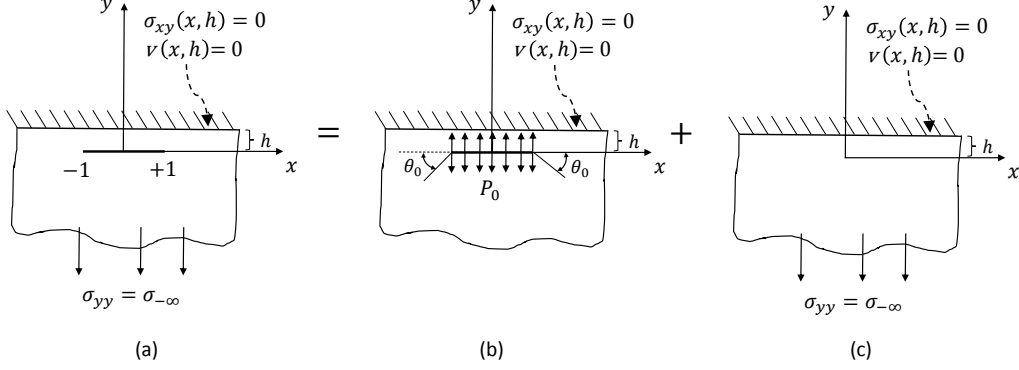
Fig. 3 (a) The solution to the problem depicted in Fig. 2(c) is obtained by superposition of (b) the solution to the problem of a uniformly pressurized crack Fig. 3(b), and (c) the solution to the problem of a semi-infinite medium, without a crack, but uniformly loaded at infinity $\sigma_{yy} = \sigma_{-\infty} = P_0$ **Fig. 3(c)**

Inasmuch as the solution to the problem depicted in Fig. 3(c) is trivially uniform (i.e., $\sigma_{yy} = \sigma_{-\infty} = P_0$ everywhere, since the fixed boundary is shear stress free), this section will focus on the solution to the problem shown in Fig. 3(b) by specializing the methods and nomenclature outlined in Erdogan and Gupta[22] for flaws in multilayered media. For a uniformly pressurized crack $\sigma_{yy}(x,0) = P_0$ on $|x| < 1$, the appropriate boundary conditions on the crack line $y = 0$, are

$$\sigma_{yy}(x,0) = -P_0(x) = P_0 \quad ; \quad |x| < 1\,,$$

$$\sigma_{xy}(x,0) = 0 \quad\quad\quad ; \quad -\infty \leq x \leq \infty\,, \tag{1}$$

$$v(x,0) = 0 \quad\quad\quad ; \quad |x| > 1\,,$$

and all components of stress and displacement vanish as $\sqrt{x^2 + y^2} \to -\infty$ (Fig. 3(b)). It is further assumed that the medium is in a state of plane strain and because of geometric and load symmetry the displacements can be written as half-range Fourier transforms of undetermined functions Φ and Ψ, that is,

$$u_i(x,y) = \frac{2}{\pi} \int_0^\infty \Phi_i(\xi, y) \sin(\xi x)\, d\xi,$$

$$\tag{2}$$

$$v_i(x,y) = \frac{2}{\pi} \int_0^\infty \Psi_i(\xi, y) \cos(\xi x)\, d\xi\,,$$

4

and here, $i = -1$ or 1, where the subscript $i = -1$ refers to fields in the infinite region below the crack line $y = 0$, and the subscript $i = 1$ to fields in the region between the crack line $y = 0$ and the rigid boundary $y = h$ illustrated in Fig. 3(b). On taking the appropriate partial derivatives of $u_i(x, y)$ and $v_i(x, y)$ in Eq. 2 and substituting them into the 2-dimensional plane strain, Cauchy-Navier equations for an isotropic elastic medium, viz.,

$$(\lambda_i + 2\mu_i)\frac{\partial^2 u_i(x, y)}{\partial x^2} + \mu_i \frac{\partial^2 u_i(x, y)}{\partial y^2} + (\lambda_i + \mu_i)\frac{\partial^2 v_i(x, y)}{\partial x \partial y} = 0\,,$$

$$(3)$$

$$\mu_i \frac{\partial^2 v_i(x, y)}{\partial x^2} + (\lambda_i + 2\mu_i)\frac{\partial^2 v_i(x, y)}{\partial y^2} + (\lambda_i + \mu_i)\frac{\partial^2 u_i(x, y)}{\partial x \partial y} = 0\,,$$

and employing Fourier's sine formula,

$$f(x) = \mathcal{F}_s\{\mathcal{F}_s(f(x) : x \to \xi); \xi \to x\} \quad 0 < x < \infty \quad, \tag{4}$$

(e.g., Eq. 1.1.5 of Titchmarsh[29]) where $\mathcal{F}_s$ denotes the half-range sine transform,

$$\mathcal{F}_s(\xi) = \mathcal{F}_s(f(x) : x \to \xi) = \sqrt{\frac{2}{\pi}} \int_0^\infty f(x) \sin(\xi x)\, dx \quad, \tag{5}$$

(e.g., Eq. 1.2.3 of Titchmarsh[29]) we arrive at the following 2 ordinary (coupled) differential equations in Φ and Ψ:

$$-K_{i1}\, \xi^2\, \Phi_i(\xi, y) + K_{i2}\, \Phi_i''(\xi, y) - \xi\, \Psi_i'(\xi, y) = 0\,,$$

$$(6)$$

$$-K_{i2}\, \xi^2\, \Psi_i(\xi, y) + K_{i1}\, \Psi_i''(\xi, y) + \xi\, \Phi_i'(\xi, y) = 0\,.$$

Here $K_{i1} = \frac{\lambda_i + 2\mu_i}{\lambda_i + \mu_i} = 2 - 2\nu_i$, and $K_{i2} = \frac{\mu_i}{\lambda_i + \mu_i} = 1 - 2\nu_i$, where λ_i and μ_i are the Lamé and shear moduli, ν_i is Poisson's ratio, and the primes, $'$, denote derivatives with respect to y. On solving Eq. 6 for $\Phi_i(\xi, y)$ we arrive at the following fourth-order ordinary differential equation:

$$\Phi_i''''(\xi, y) - 2\, \xi^2\, \Phi_i''(\xi, y) + \Phi_i(\xi, y) = 0 \quad, \tag{7}$$

with general solution,

$$\Phi_i(\xi, y) = (A_{i1} + A_{i2})e^{-\xi y} + (A_{i3} + A_{i4})e^{\xi y} \quad. \tag{8}$$

On substituting Eq. 8, and its second derivative into Eq. 6_1, and integrating $\Psi_i'(\xi, y)$ over all y results in the general solution for $\Psi_i(\xi, y)$,

$$\Psi_i(\xi, y) = (A_{i1} + (\frac{\kappa_i}{\xi} + y)A_{i2})e^{-\xi y} + (-A_{i3} + (\frac{\kappa_i}{\xi} - y)A_{i4})e^{\xi y} \quad, \qquad (9)$$

where $\kappa_i = 3 - 4\nu_i$. In these equations, the $A_{ij} = A_{ij}(\xi), i = -1$ or 1, and $j = 1, ..., 4$ are to be determined from the boundary and continuity conditions for the specific problem. On substituting Eq. 8 and Eq. 9 into Eq. 2 we arrive at the general expressions for the displacements, given without derivation in Erdogan and Gupta,[22]

$$u_i(x, y) = \frac{2}{\pi} \int_0^\infty \{(A_{i1} + A_{i2})e^{-\xi y} + (A_{i3} + A_{i4})e^{\xi y}\} \sin(\xi x)\, d\xi,$$

(10)

$$v_i(x, y) = \frac{2}{\pi} \int_0^\infty \{(A_{i1} + (\frac{\kappa_i}{\xi} + y)A_{i2})e^{-\xi y} - (A_{i3} - (\frac{\kappa_i}{\xi} - y)A_{i4})e^{\xi y}\} \cos(\xi x)\, d\xi \,.$$

The normal $\sigma_{yy}^i(x, y)$ and shear $\sigma_{xy}^i(x, y)$ stresses follow immediately by taking the appropriate derivatives of Eq. 10 and substitution into Hooke's law written in Cartesian coordinates,

$$\sigma_{yy}^i(x, y) = (\lambda_i + 2\mu_i)\frac{\partial v_i(x, y)}{\partial y} + \lambda_i\frac{\partial u_i(x, y)}{\partial x} \,,$$

(11)

$$\sigma_{xy}^i(x, y) = \mu_i(\frac{\partial u_i(x, y)}{\partial y} + \frac{\partial v_i(x, y)}{\partial x}) \,,$$

which results in

$$\frac{\sigma_{yy}^i(x, y)}{2\mu_i} = \frac{2}{\pi} \int_0^\infty \{-[\xi(A_{i1} + A_{i2}y) + 2(1 - \nu_i)A_{i2}]e^{-\xi y}$$

$$+ [-\xi(A_{i3} + A_{i4}y) + 2(1 - \nu_i)A_{i4}]e^{\xi y}\} \cos(\xi x)\, d\xi,$$

(12)

$$\frac{\sigma_{xy}^i(x, y)}{2\mu_i} = \frac{2}{\pi} \int_0^\infty \{-[\xi(A_{i1} + A_{i2}y) + (1 - 2\nu_i)A_{i2}]e^{-\xi y}$$

$$+ [\xi(A_{i3} + A_{i4}y) - (1 - 2\nu_i)A_{i4}]e^{\xi y}\} \sin(\xi x)\, d\xi \,.$$

3. Boundary and Continuity Conditions

The geometry for this problem can be envisioned as consisting of 2 simply connected regions: one region consists of an isotropic elastic strip of width h, where $0 \leq y \leq h$ and $-\infty < x < \infty$, that is bonded to another region that consists of a semi-infinite isotropic elastic plane, where $-\infty < y \leq 0$ and $-\infty < x < \infty$. The bond connecting the first region to the second region occurs along $y = 0$, and all x, except for $|x| < 1$ (see Fig. 3(b)). Eight constants are required to solve this problem, 4 for the strip and 4 for the semi-infinite plane. Two constants, A_{-11} and A_{-12} are identically zero for the displacements to be bounded as $y \to -\infty$. This leaves 6 constants to be determined from the following 6 conditions:

$$
\begin{aligned}
&1) \quad \sigma_{xy}^1(x, h) = 0 &&; \quad y = h\,, \\[2mm]
&2) \quad v_1(x, h) = 0 &&; \quad y = h\,, \\[2mm]
&3) \quad \sigma_{yy}^1(x, 0) - \sigma_{yy}^{-1}(x, 0) = 0 &&; \quad y = 0\,, \\[2mm]
&4) \quad \sigma_{xy}^1(x, 0) - \sigma_{xy}^{-1}(x, 0) = 0 &&; \quad y = 0\,, \\[2mm]
&5) \quad \frac{\partial(u_1 - u_{-1})}{\partial x} = f_1\,\delta(x - t) &&; \quad y = 0\,, \\[2mm]
&6) \quad \frac{\partial(v_1 - v_{-1})}{\partial x} = f_2\,\delta(x - t) &&; \quad y = 0\,.
\end{aligned}
\tag{13}
$$

Equations 13_1 and 13_2 are the stress boundary conditions on the upper strip rigid boundary depicted in Fig. 3(b). Equations 13_3 and 13_4 are the stress continuity conditions on the crack line. Equations 13_5 and 13_6 represent the symmetrically disposed unit dislocations at $y = 0$, $x = t$. In the present problem, therefore, a 6×6 system is inverted, which provides expressions for A_{11}, A_{12}, A_{13}, A_{14}, A_{-13}, A_{-14} as functions of f_1, f_2, and ξ. The system of equations are derived by substitution of Eq. 10 and Eq. 12 into Eq. 13, the result of which appears in matrix-vector form as

$$
A\,\vec{x} = \vec{b}\ ,
\tag{14}
$$

where

$$
A = \begin{bmatrix}
e^{-h\xi} & e^{-h\xi}\left(h+\frac{\kappa}{\xi}\right) & -e^{h\xi} & e^{h\xi}\left(\frac{\kappa}{\xi}-h\right) & 0 & 0 \\
-e^{-h\xi}\xi & e^{-h\xi}(2\nu-h\xi-1) & e^{h\xi}\xi & e^{h\xi}(2\nu+h\xi-1) & 0 & 0 \\
-\xi & -2(1-\nu) & -\xi & 2(1-\nu) & \xi & -2(1-\nu) \\
-\xi & 2\nu-1 & \xi & 2\nu-1 & -\xi & 1-2\nu \\
\xi & 0 & \xi & 0 & -\xi & 0 \\
-\xi & -\kappa & \xi & -\kappa & -\xi & \kappa
\end{bmatrix} , (15)
$$

and we have dropped the subscript i in this equation since the elastic material above and below the crack line is assumed, for this problem, to be identical (i.e., $\nu = \nu_1 = \nu_{-1}$, and $\kappa = 3 - 4\nu$), while

$$
\vec{x} = \begin{bmatrix} A_{11} \\ A_{12} \\ A_{13} \\ A_{14} \\ A_{-13} \\ A_{-14} \end{bmatrix} , \quad \vec{b} = \begin{bmatrix} 0 \\ 0 \\ 0 \\ 0 \\ f_1\cos(\xi t) \\ f_2\sin(\xi t) \end{bmatrix} . \tag{16}
$$

The expressions for the $\vec{x} = A_{ij}(\xi)$ are obtained by finding the inverse of matrix Eq. 15, $\vec{x} = A^{-1}\vec{b}$, viz.,

$$
\vec{x} = \begin{bmatrix}
\frac{\cos(t\xi)f_1}{2\xi} + \frac{(1-2\nu)\sin(t\xi)f_2}{2(-1+k+2\nu)\xi} \\[2mm]
\frac{\cos(t\xi)f_1}{-4+4\nu} + \frac{\sin(t\xi)f_2}{2-2k-4\nu} \\[2mm]
\frac{e^{-2h\xi}(-1+\nu+h\xi)\cos(t\xi)f_1}{2(-1+\nu)\xi} + \frac{e^{-2h\xi}(1-2\nu-2h\xi)\sin(t\xi)f_2}{2(-1+k+2\nu)\xi} \\[2mm]
\frac{e^{-2h\xi}\cos(t\xi)f_1}{2(2-2\nu)} + \frac{e^{-2h\xi}\sin(t\xi)f_2}{2(-1+k+2\nu)} \\[2mm]
\frac{\left(-1+\frac{e^{-2h\xi}(-1+\nu+h\xi)}{-1+\nu}\right)\cos(t\xi)f_1}{2\xi} + \frac{e^{-2h\xi}\left(1+e^{2h\xi}(1-2\nu)-2\nu-2h\xi\right)\sin(t\xi)f_2}{2(-1+k+2\nu)\xi} \\[2mm]
\frac{\left(-1+e^{-2h\xi}\right)\cos(t\xi)f_1}{4-4\nu} + \frac{\left(1+e^{-2h\xi}\right)\sin(t\xi)f_2}{2(-1+k+2\nu)}
\end{bmatrix} . \tag{17}
$$

A compact expression for the representation of the $A_{ij}(\xi)$ in Eq. 17 is

$$A_{ij}(\xi) = F_{ij}^1(\xi) f_1 \cos(\xi t) + F_{ij}^2(\xi) f_2 \sin(\xi t),$$

$$(18)$$

$$(i = -1, 1, \; j = 1, ..., 4),$$

where the F_{ij}^i are functions of the elastic properties and ξ. On substituting Eq. 18 into Eq. 12 gives the 2 stress components σ_{yy} and σ_{xy} due to the 2 unit dislocations f_1 and f_2 given by Equations 13_5 and 13_6 in the upper strip as

$$\sigma_{yy}(x, y, t) = h_{11}(x, y, t) f_1 + h_{12}(x, y, t) f_2,$$

$$(19)$$

$$\sigma_{xy}(x, y, t) = h_{21}(x, y, t) f_1 + h_{22}(x, y, t) f_2.$$

Equation 19 represents the Green's functions for the current problem and the h_{ij} are singular integrals involving the F_{ij}^i. Assuming now that the unit dislocations, f_1 and f_2, are functions of t and represent the unknown distributions of dislocations on the crack, the integral expressions of Eq. 19 for the determination of $f_1(t)$ and $f_2(t)$ become

$$\lim_{y \to 0} \int_0^1 h_{11}(x, y, t) f_1(t) + h_{12}(x, y, t) f_2(t) \, dt = \sigma_{yy}(x),$$

$$(20)$$

$$\lim_{y \to 0} \int_0^1 h_{21}(x, y, t) f_1(t) + h_{22}(x, y, t) f_2(t) \, dt = \sigma_{xy}(x),$$

$$0 \le x < 1,$$

or

$$\frac{4(\nu - 1)}{2\mu} \sigma_{yy}(x, 0) = \frac{1}{\pi} \int_{-1}^1 f_1(t) \, dt \int_0^\infty -2h\xi \cos((t - x)\xi) e^{-2h\xi} \, d\xi$$

$$+ \frac{1}{\pi} \int_{-1}^1 f_2(t) \, dt \int_0^\infty -(1 + 2h\xi) \sin((t - x)\xi) e^{-2h\xi} \, d\xi \qquad (21)$$

$$- \lim_{y \to 0} \frac{1}{\pi} \int_{-1}^1 f_2(t) \, dt \int_0^\infty \sin((t - x)\xi) e^{-y\xi} \, d\xi,$$

and

$$\frac{4\,(\nu-1)}{2\,\mu}\,\sigma_{xy}(x,0) = -\frac{1}{\pi}\int_{-1}^{1} f_2(t)\,dt \int_0^\infty -2h\xi\cos((t-x)\xi)e^{-2h\xi}d\xi$$

$$-\frac{1}{\pi}\int_{-1}^{1} f_1(t)\,dt \int_0^\infty (1-2h\xi)\sin((t-x)\xi)e^{-2h\xi}d\xi \tag{22}$$

$$+\lim_{y\to 0}\frac{1}{\pi}\int_{-1}^{1} f_1(t)\,dt \int_0^\infty \sin((t-x)\xi)e^{-y\xi}d\xi\,.$$

Integration of the sine and cosine transforms in the iterated integrals in Eq. 21 and Eq. 22 results in

$$\frac{1}{\pi}\int_{-1}^{1}\frac{f_1(t)}{t-x}dt + \frac{1}{\pi}\int_{-1}^{1} k_{11}(x,t)\,f_1(t) + k_{12}(x,t)\,f_2(t)dt = 0\,,$$

$$\frac{1}{\pi}\int_{-1}^{1}\frac{f_2(t)}{t-x}dt + \frac{1}{\pi}\int_{-1}^{1} k_{21}(x,t)\,f_1(t) + k_{22}(x,t)\,f_2(t)dt = \frac{-(\kappa+1)P_0}{2\mu}\,, \tag{23}$$

$$-1 < x < 1\,.$$

In the derivation of Eq. 23 we have assumed that the applied normal stress $\sigma_{yy}(x,0)$ on the crack is constant and the applied shear stress $\sigma_{xy}(x,0)$ on the crack is zero. In addition, the unknown dislocation densities f_1, f_2 in Eq. 23 are written as the tangential derivatives of the relative crack displacements, as

$$f_1(x) = \frac{\partial[u_1(x) - u_{-1}(x)]}{\partial x}\,,\quad f_2(x) = \frac{\partial[v_1(x) - v_{-1}(x)]}{\partial x}\,,$$

$$\sigma_{xy}(x,0) = 0\,,\quad \sigma_{yy}(x,0) = -P_0\frac{(1+\kappa)}{2\mu}\,, \tag{24}$$

$$-1 < x < 1\,.$$

The kernel functions in Eq. 23 are symmetric $k_{ij} = k_{ji}$ and are derived herein for the specific problem illustrated in Fig. 3(b) as

$$k_{11}(x,t) = \frac{\left(4h^2 - (t-x)^2\right)(t-x)}{\left(4h^2 + (t-x)^2\right)^2},$$

$$k_{12}(x,t) = k_{21}(x,t) = \frac{2h\left(4h^2 - (t-x)^2\right)}{\left(4h^2 + (t-x)^2\right)^2}, \tag{25}$$

$$k_{22}(x,t) = \frac{\left(12h^2 + (t-x)^2\right)(t-x)}{\left(4h^2 + (t-x)^2\right)^2}.$$

The unknown dislocation densities $f_1(t)$ and $f_2(t)$ are numerically determined by reducing the singular integrals in Eq. 23 to an infinite system of linear algebraic equations using the orthogonality properties of the Chebyshev polynomials.[23] It is common practice to write the dislocation densities in terms of an infinite series, truncated at the $k = N^{th}$ term, of Chebyshev polynomials of the first kind,[*]

$$f_1(t) = \frac{1}{\sqrt{1-t^2}} \sum_{k=1}^{\infty} A_k \, T_{2k}(t),$$

$$\tag{26}$$

$$f_2(t) = \frac{1}{\sqrt{1-t^2}} \sum_{k=1}^{\infty} B_k \, T_{2k-1}(t).$$

On substituting Eq. 26 into Eq. 23, and using the orthogonality conditions of the Chebyshev polynomials, one can derive a set of functional equations involving the unknown constants A_k and B_k (cf. Eq. (7.97) of Erdogan et al.[23]). The functional equations can be solved using a weighted residual method to arrive at the following

---

[*]The more general Jacobi polynomials $P_k^{(\alpha,\beta)}$ are used in solutions to problems where $f(t) = g(t)(1-t)^\alpha(t+1)^\alpha$ in Eq. 23 and $g(t) = \sum_{k=0}^{\infty} B_k P_k^{(\alpha,\beta)}$; since the solution of Eq. 23 has integrable singularities at the end points, then $\alpha = \beta = -1/2$, and the Jacobi polynomials coincide with the Chebyshev polynomials of the first kind used in Eq. 26 (cf. discussion on pages 380–381 of Erdogan et al.[23]).

system equations:

$$\frac{\pi}{2} A_k + \sum_{n=1}^{N} (a_{kn} A_n + b_{kn} B_n) = F_{1k},$$

$$\frac{\pi}{2} B_k + \sum_{n=1}^{N} (c_{kn} A_n + d_{kn} B_n) = F_{2k},$$

$$F_{1k} = 0, \quad (k = 1, ...N),$$

$$F_{21} = -\frac{\pi}{2} P_0 \frac{\kappa + 1}{2\mu}, \quad F_{2k} = 0, \quad (k = 2, ...N),$$

where the definitions of constants a_{kn}, b_{kn}, c_{kn}, and d_{kn} can be found in Appendix A.

4.   Stress Intensity Factors

In this section, SIFs are computed and compared with the prior results of Chang and Ma[25] who tabulate their results that are based on the Schwarz-Neumann alternating technique,[24] along with those of Yokobori et al.,[26] and Kamei and Yokobori[27] (Table 1). Using the formalism developed in this report, the mode I, k_1, and mode II, k_2, SIFs can be written in a straightforward manner, cf. page 394 of Erdogan et al.,[23] as

$$k_1 = -\frac{2\mu}{1+\kappa} \sum_{k=1}^{\infty} B_k, \quad \text{and} \quad k_2 = -\frac{2\mu}{1+\kappa} \sum_{k=1}^{\infty} A_k \qquad (28)$$

where the infinite series is normally truncated to a finite number of terms, N, say $k = N = 9$, and the A_k and B_k are given in Eq. A-7. One immediately observes from Table 1 that the SIFs obtained by the prior authors using different solution methodologies agree quite well with our own results* for the case $N = 9$, cf. Appendix B that illustrates SIF convergence for $N = 3, 6, 9$ and various values of a/h. In general, as $a/h \to 0$, that is, as the crack distance from the rigid boundary increases, the mode II stress intensity factor approaches zero, $k_2 \to 0$, and the mode

---

*We use the Erdogan et al.[23] convention for the shear stress so that our F_{II} values are opposite in sign to that used by the other authors, but consistent with those computed using Abaqus in section 8.

I stress intensity factor approaches unity, $k_1 \to 1^*$. Since the SIFs derived by earlier authors for the 2 overlapping parallel crack problem under remote tension are nearly the same as our problem of a single crack parallel to a rigid boundary under remote tension Table 1, these 2 problems are, therefore, mechanically equivalent.

The equation used to derive the initial angle of crack growth (see Table 1) subjected to mixed-mode loading is written as a function of k_1 and k_2, and given by Eq. 1 on page 236 of Erdogan[31] as

$$k_1 \sin \theta_0 + k_2(3 \cos \theta_0 - 1) = 0 . \tag{29}$$

For cracks that are distant from the rigid boundary, the initial angle of crack growth (cleavage angle) approaches zero, $\theta_0 \to 0$, the crack propagation is self-similar; cracks that approach the rigid boundary propagate at ever increasing angles (see Fig. 4) relative to the crack line, and away from the rigid boundary (see Fig. 3(b)).

Table 1 Normalized SIFs for 2 parallel cracks in an infinite plane under remote tension, where $K_I = F_I \sigma \sqrt{\pi a}$, $K_{II} = F_{II} \sigma \sqrt{\pi a}$, and $k_1 = F_I$; $k_2 = F_{II}$ are determined using Eq. 28

a/h	F_I[26,27]	F_I[25]	F_I[a]	F_{II}[25]	F_{II}[a]	θ_0[b]
0.01	...	...	0.99996	...	-1.8747×10^{-7}	0
0.1	...	...	0.9963	...	–0.00018	0.02
0.2	0.9855[26]	0.9858	0.9857	0.0014	–0.0014	0.16
0.4	0.9508[26]	0.9505	0.9505	0.0094	–0.0094	1.13
0.6	0.9089[26]	0.9092	0.9086	0.0246	–0.0246	3.09
0.8	0.8727[26]	0.8722	0.8706	0.0431	–0.0429	5.61
1.0	0.8319[27]	0.8431	0.8403	0.0611	–0.0607	8.18
1.25	0.8037[27]	0.8166	0.8131	0.0803	–0.0793	10.94
$1.\overline{66}$	...	...	0.7860	...	–0.1011	14.21
2.0	0.7569[27]	0.7734	0.7737	0.1166	–0.1128	15.95
5.0	...	...	0.7445	...	–0.1567	22.02
10.0	...	...	0.7385	...	–0.1792	24.74

[a] F_I and F_{II} values are from Table B-1, $N = 9$.
[b] θ_0 values are derived using F_I and F_{II} values in this Table 1.

---

*Some authors use the convention $K_I \to \sigma \sqrt{\pi a}$ as $a/h \to \infty$ but we use the normalized constant $k_1 \to \sigma \sqrt{a}$ as $a/h \to \infty$, cf. footnote 2 of Erdogan.[30]
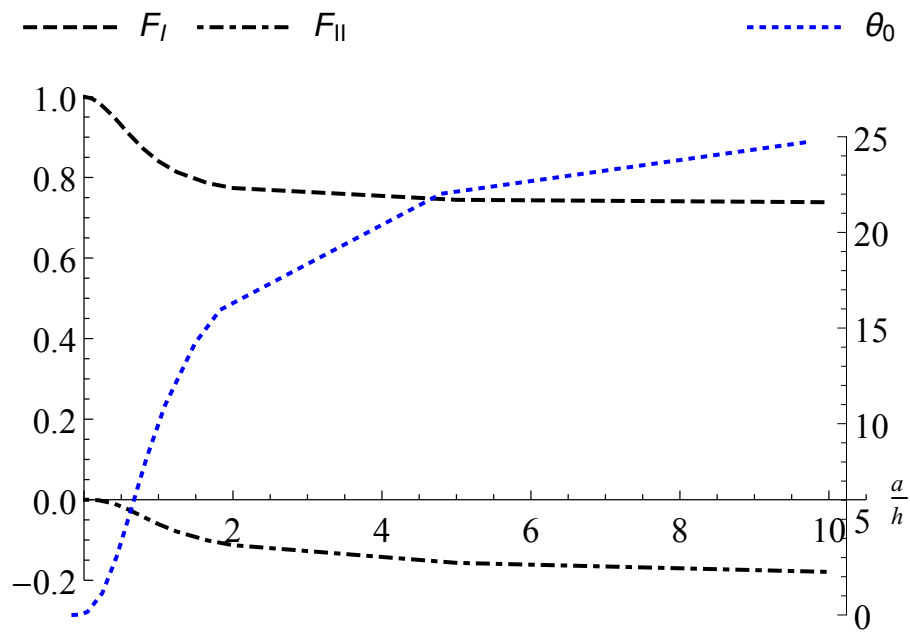
Fig. 4 F_I, F_{II}, **and cleavage angles** θ_0 **vs.** a/h **from Table 1 for a crack parallel to a rigid boundary under symmetric loading**

5. Normal and Shear Stresses

In this section, we determine the normal $\sigma_{yy}(x, h_1)$ and shear stress $\sigma_{xy}(x, h_1)$ at $y = h_1$, where $0 \leq h_1 \leq h$ and compare our results with those obtained using the Abaqus commercial FE code where the crack is modeled using the XFEM.

On substituting the $A_{ij}(\xi)$ from Eq. 17 into Eq. 12 we arrive at the iterated integrals for the normal $\sigma_{yy}(x, h_1)$ and shear stress $\sigma_{xy}(x, h_1)$:

$$\frac{-(\kappa + 1)}{2\mu} \sigma_{yy}(x, h_1) =$$

$$\frac{1}{\pi} \int_{-1}^{1} f_1(t) \, dt \int_{0}^{\infty} e^{-(2h+h_1)\xi} \left(-e^{2h\xi} h_1 + e^{2h_1\xi}(-2h + h_1) \right) \xi \cos((t - x)\xi) \, d\xi$$

$$+ \frac{1}{\pi} \int_{-1}^{1} f_2(t) \, dt \int_{0}^{\infty} e^{-(2h+h_1)\xi} \left(-e^{2h\xi}(1 + h_1\xi) - e^{2h_1\xi}(1 + 2h\xi - h_1\xi) \right) \sin(\xi(t - x)) \, d\xi$$

$$(30)$$

$$\frac{-(\kappa + 1)}{2\mu} \sigma_{xy}(x, h_1) =$$

$$\frac{1}{\pi} \int_{-1}^{1} f_1(t) \, dt \int_{0}^{\infty} -e^{-(2h+h_1)\xi} \left(e^{2h\xi}(-1 + h_1\xi) + e^{2h_1\xi}(1 - 2h\xi + h_1\xi) \right) \sin((t - x)\xi) \, d\xi$$

$$+ \frac{1}{\pi} \int_{-1}^{1} f_2(t) \, dt \int_{0}^{\infty} -e^{-(2h+h_1)\xi} \left(e^{2h\xi} h_1 + e^{2h_1\xi}(-2h + h_1) \right) \xi \cos((t - x)\xi) \, d\xi \, .$$

On integrating the sine and cosine transforms in Eq. 30 we arrive at the following equations for the normal stress $\sigma_{yy}(x, h_1)$:

$$\frac{-(\kappa + 1)}{2\mu}\sigma_{yy}(x, h_1) = \frac{1}{\pi} \int_{-1}^{1} f_1(t) \{ \frac{h_1\left(-h_1^2 + (t - x)^2\right)}{\left(h_1^2 + (t - x)^2\right)^2}$$

$$+\frac{h_1\left((-2h + h_1)^2 - (t - x)^2\right)}{\left((-2h + h_1)^2 + (t - x)^2\right)^2} + \frac{2h\left(-(-2h + h_1)^2 + (t - x)^2\right)}{\left((-2h + h_1)^2 + (t - x)^2\right)^2}\}dt$$

$$-\frac{1}{\pi} \int_{-1}^{1} f_2(t)\{\frac{2h_1^2}{\left(h_1^2 + (t - x)^2\right)^2} + \frac{1}{h_1^2 + (t - x)^2}$$

$$+\frac{2(-2h + h_1)^2}{\left((-2h + h_1)^2 + (t - x)^2\right)^2} + \frac{1}{(-2h + h_1)^2 + (t - x)^2}\}(t - x)dt,$$

(31)

and shear stress $\sigma_{xy}(x, h_1)$ in terms of polynomials in x and t,

$$\frac{-(\kappa + 1)}{2\mu}\sigma_{xy}(x, h_1) = \frac{1}{\pi} \int_{-1}^{1} f_1(t) \{ \frac{-2h_1^2}{\left(h_1^2 + (t - x)^2\right)^2} + \frac{1}{h_1^2 + (t - x)^2}$$

$$+\frac{2(-2h + h_1)^2}{\left((-2h + h_1)^2 + (t - x)^2\right)^2} - \frac{1}{(-2h + h_1)^2 + (t - x)^2}\}(t - x)dt$$

(32)

$$+\frac{1}{\pi} \int_{-1}^{1} f_2(t)\{-\frac{h_1\left((-2h + h_1)^2 - (t - x)^2\right)}{\left((-2h + h_1)^2 + (t - x)^2\right)^2}$$

$$+\frac{2h\left(-(-2h + h_1)^2 + (t - x)^2\right)}{\left((-2h + h_1)^2 + (t - x)^2\right)^2} + \frac{h_1(h_1 + t - x)(h_1 - t + x)}{\left(h_1^2 + (t - x)^2\right)^2}\}dt.$$

On substituting the dislocation densities given by Eq. 26 into Eq. 31 and Eq. 32 together with the A_k, and B_k determined by the methods described in Appendix A, and employing Gauss-Chebyshev numerical integration using Eq. A-3, we arrive at the normal* $\sigma_{yy}(x, h_1)$ and shear stress $\sigma_{xy}(x, h_1)$ distributions for $0 \leq h_1 \leq h$ along line $0 \leq x \leq 5$, where they are compared with the Abaqus commercial

---

*Recall that the normal stress distribution depicted in Fig. 3(a) consists of superposing Eq. 31 with a unit remote stress at infinity $\sigma_{yy} = \sigma_{-\infty} = 1$.

FE solutions (Figs. 5 and 6). Also, the normal stress approaches the far-field unit applied tensile stress in Fig. 5 and far-field null shear stress in Fig. 6.

In Section 6, we verify the accuracy of the Gauss-Chebyshev solutions depicted in Figs. 5 and 6 by showing they are within machine precision of analytical solutions for the problem of a crack in an infinite plane subjected to remote tension. This result allows us to accurately estimate the error between our solutions and those obtained using Abaqus. Finally, we show in Fig. 7 that for all parallel cracks that are in close proximity to each other, (i.e., at normalized distances $a/h > 0.95$), the stress between the parallel cracks is compressive (stress is negative in compression), and the compressive stress increases linearly in magnitude with normalized distance a/h (Fig. 7).
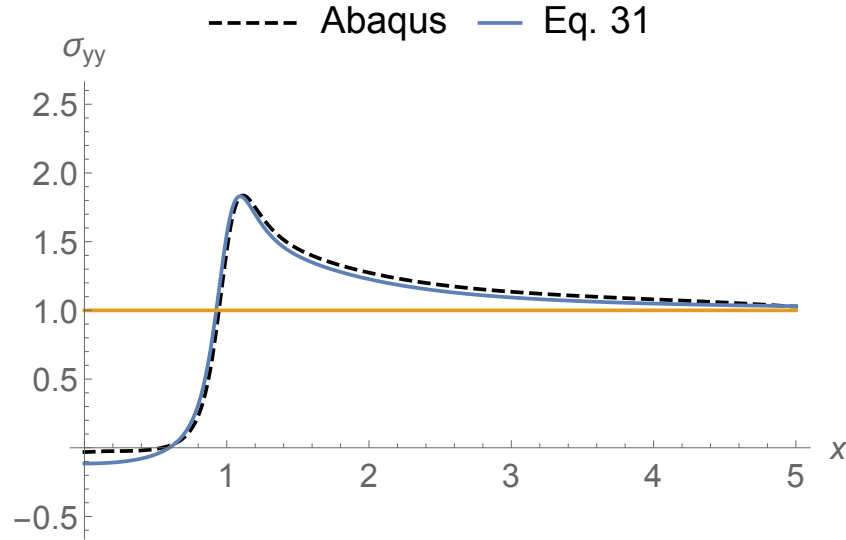
Fig. 5 Normal stress $\sigma_{yy}(x, h_1)$ solution for the boundary value problem depicted in Fig. 3(a): Abaqus simulation compared with Eq. 31 for $h = 0.6$ and $h_1 = 0.2$; with $A_1, ... A_N, B_1, ..., B_N$ constants, $k = N = 6$ in Eq. 26
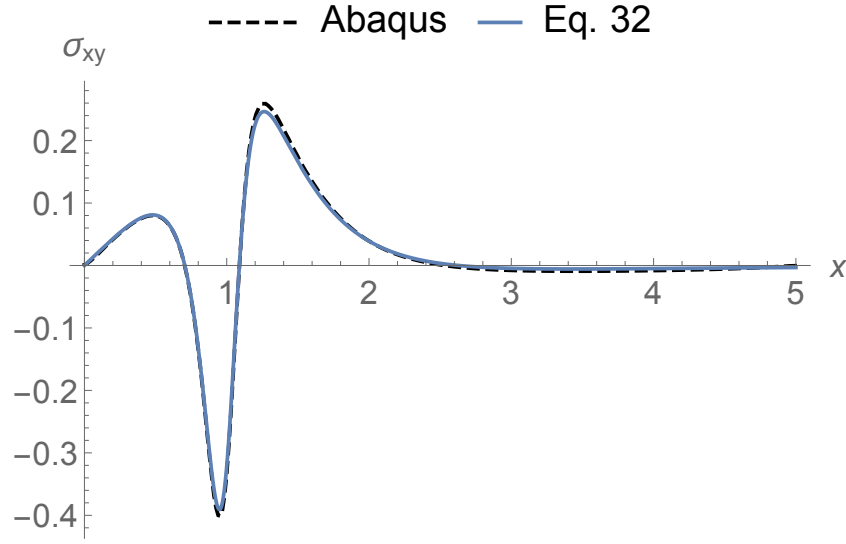
Fig. 6 Shear stress $\sigma_{xy}(x, h_1)$ solution for the boundary value problem depicted in Fig. 3(a): Abaqus simulation compared with Eq. 32 for $h = 0.6$ and $h_1 = 0.2$; with $A_1, ... A_N, B_1, ..., B_N$ constants, $k = N = 6$ in Eq. 26
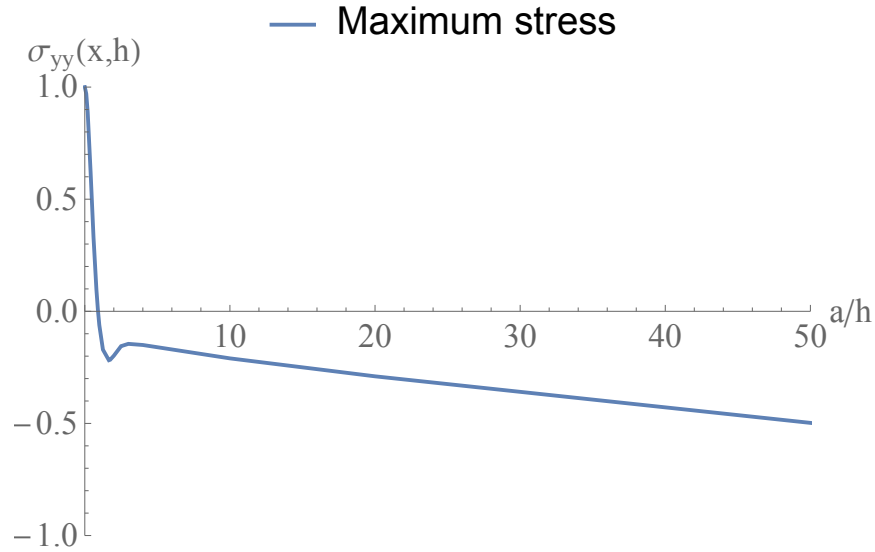
Fig. 7 Maximum stress $\sigma_{yy}(x, h)$ along rigid boundary line $y = h$ vs. a/h; far-field tensile stress is $\sigma_{yy}(x, -\infty) = 1$ with tension positive, compression negative. At $a/h \approx 0.95$ the stress changes from tension to compression and then increases linearly with a/h.

6. Verification of Our Derived Solutions

In this section, we verify the accuracy of our derived solutions and the Gauss-Chebyshev numerical integration methodology against a closed-form solution for the normal and shear stress distributions in an infinite plate containing a crack subjected to a remote tensile stress $\sigma_{yy}(x, \infty) = \sigma_\infty = 1$. The normalized analytical solution for the stress fields is given in Zehnder,[28]

$$\frac{\sigma_{yy}(x, y)}{\sigma_\infty} = \Re\left(\frac{z}{\sqrt{z^2 - 1}}\right) + y\Im\left(\frac{1}{\sqrt{z^2 - 1}} - \frac{z^2}{(z^2 - 1)^{3/2}}\right), \qquad (33)$$

and

$$\frac{\sigma_{xy}(x, y)}{\sigma_\infty} = y\Re\left(\frac{1}{\sqrt{z^2 - 1}} - \frac{z^2}{(z^2 - 1)^{3/2}}\right), \qquad (34)$$

where $z = x + i\,y$, and $\Re$ denotes the real part, and $\Im$ the imaginary part of the quantity in parentheses. These solutions are plotted in Figs. 8 and 9. The accuracy of our derived normal stress, Eq. 31, and shear stress, Eq. 32, solutions is determined by specializing the solutions to the case when the crack is distant from the rigid boundary (e.g., at $y = h = 1000$), but the stress distribution is evaluated close to the crack line $y = 0$, (i.e., at a distance $y = h_1 = 0.1$). We compute the relative error[32] between our Gauss-Chebyshev numerical solution and the exact analytical solution[28] for the case of a crack in an infinite plane subjected to a remote tensile stress. If $\Sigma(x, h_1)$ represents the exact value of the stress given by Eq. 33 or Eq. 34 and $\widetilde{\Sigma}(x, h_1)$ represents the approximate value of the corresponding stress using Gauss-Chebyshev numerical integration, then the relative error is given as

$$\text{relerr} = 1 - \widetilde{\Sigma}(x, h_1)/\Sigma(x, h_1). \qquad (35)$$

Illustrations of $\text{Log}_{10}(|\text{relerr}|)$, where $|\text{relerr}|$ denotes the absolute value of relerr, for the normal and shear stress distributions appear in Figs. 10 and 11 with oscillatory solution accuracy ranging from 10 to 20 significant digits using $n = 100$ terms and averaging about 15 significant digits using $n = 300$ terms in the numerical integration Eq. A-3. The relative error is defined only if $\Sigma(x, h_1) \neq 0$, since if $\Sigma(x, h_1) = 0$ the error becomes unbounded; a loss in precision is indicated by the arrow in Fig. 11 (for $n = 300$) at an x-position where the shear stress passes through a zero point on the ordinate in Fig. 9. The relative error for the shear stress is rescaled and plotted for the $n = 300$ case in Fig. 12. It is clear that the relative

error between our derived normal stress, Eq. 31, and shear stress, Eq. 32, solutions and the exact analytical solutions is at machine precision using double precision arithmetic in Mathematica[33] with approximately 15 significant digits in the solution, cf. pg. 253, Table 7.1 of Oberkampf and Roy.[34]
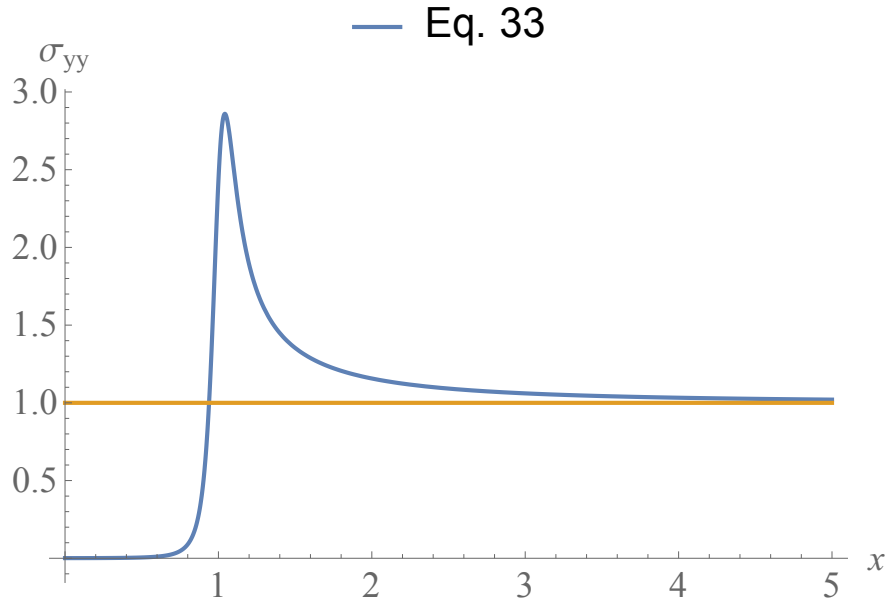
Fig. 8 **Exact normal stress $\sigma_{yy}(x, y)$ distribution at $y = 0.1$ (Eq. 33) in an infinite plate containing a crack subjected to a remote stress at $y = \pm\infty$**
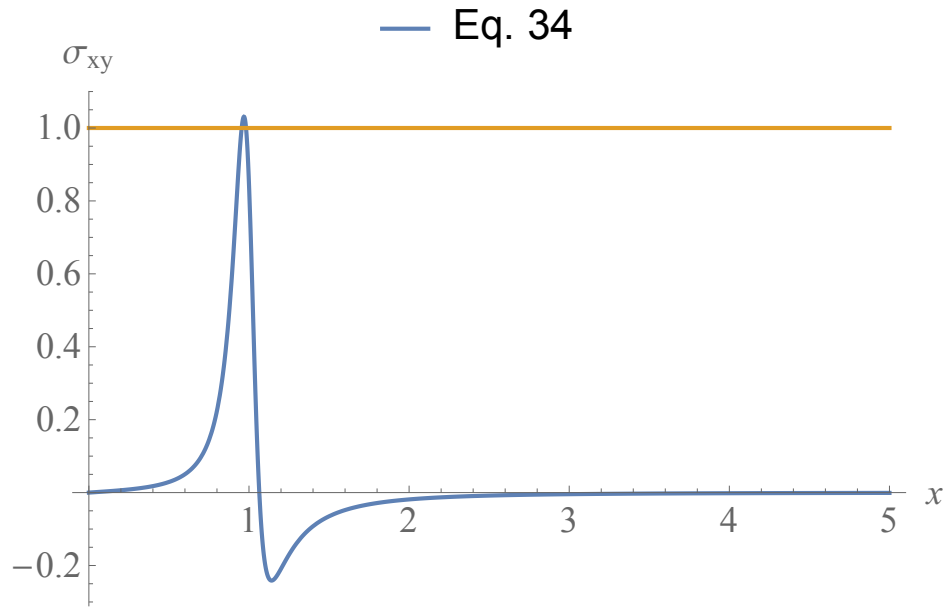
Fig. 9 **Exact shear stress** $\sigma_{xy}(x, y)$ **distribution at** $y = 0.1$ **(Eq. 34) in an infinite plate containing a crack subjected to a remote stress at** $y = \pm\infty$
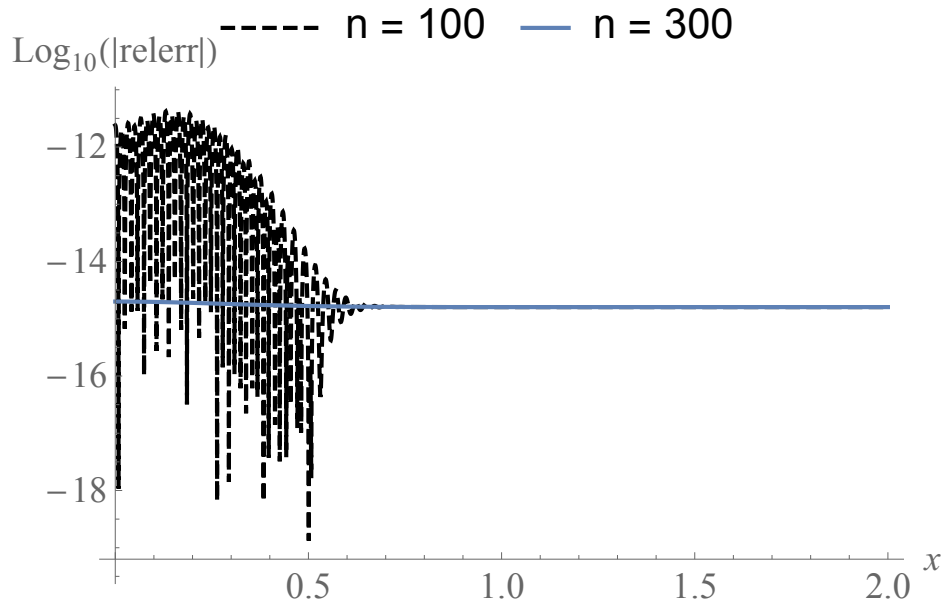
Fig. 10 **Numerical accuracy of the normal stress determined with Gauss-Chebyshev numerical integration relative to the exact solution shown in Fig. 8 over the space interval** $0 \leq x \leq 2$**; over this interval, the numerical solution accuracy ranges from 12 to 18 significant digits for** $n = 100$ **terms and averages 15 significant digits for** $n = 300$ **terms in Eq. A-3; with** $A_1, ...A_N, B_1, ..., B_N$ **constants,** $k = N = 9$ **in Eq. 26**

21
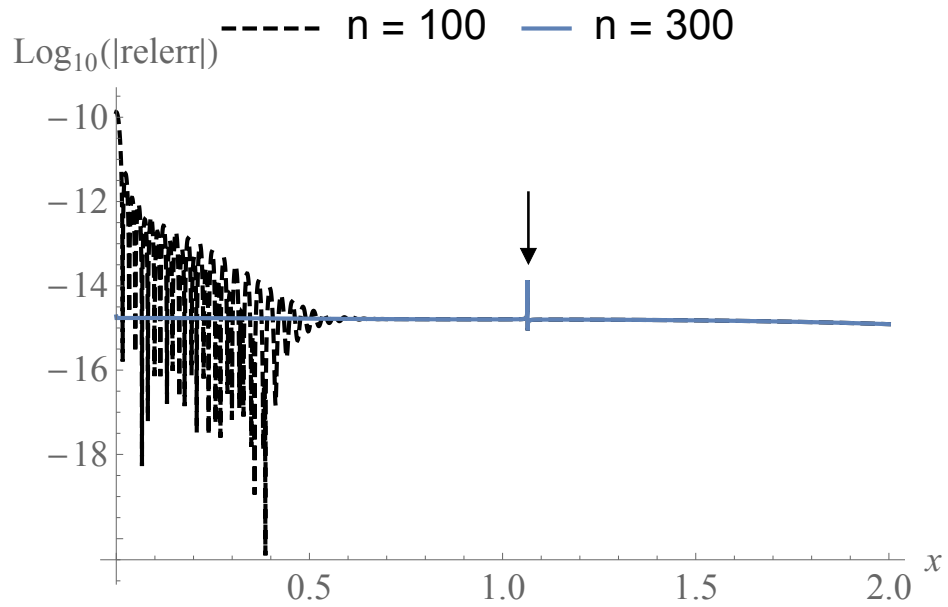
Fig. 11 Numerical accuracy of the shear stress determined with Gauss-Chebyshev numerical integration relative to the exact solution shown in **Fig. 9** over the space interval $0 \leq x \leq 2$; over this interval, the numerical solution accuracy ranges from **10 to 20 significant digits for** $n = 100$ **terms and averages 15 significant digits for** $n = 300$ **terms in Eq. A-3; with** $A_1, ... A_N, B_1, ..., B_N$ **constants,** $k = N = 9$ **in Eq. 26**
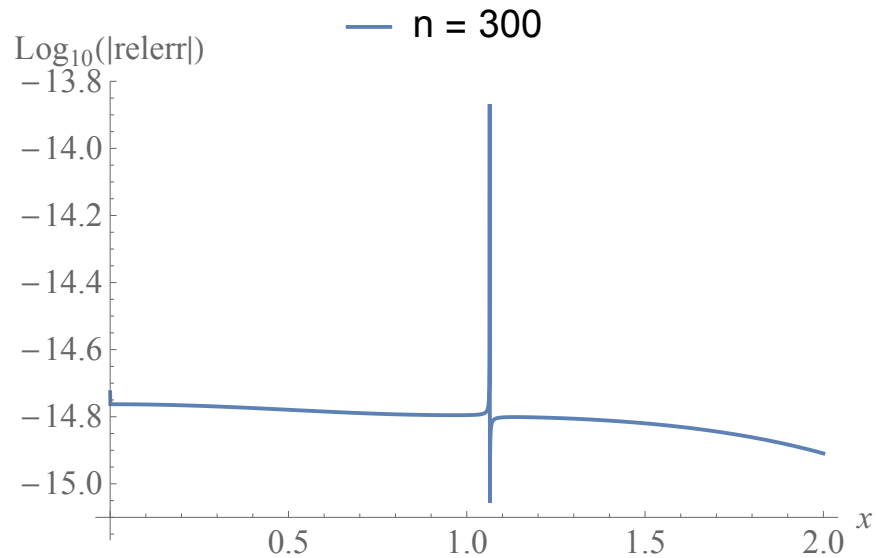
Fig. 12 Rescaled numerical accuracy of the shear stress for $n = 300$ terms shown in **Fig. 11**

7. Relative Error in the Abaqus Simulations

Earlier in Section 6, we demonstrated that our numerical solutions are at machine precision using double precision arithmetic in Mathematica.[33] In this section we will evaluate the accuracy of the normal and shear stress simulations illustrated in Figs. 5 and 6 that were determined using the Abaqus FE code. This can accomplished by evaluating Eq. 31 and Eq. 32 at the same $(x, y = 0.2)$ coordinate locations as those used in the Abaqus simulations, and calculating the relative error using Eq. 35.

Figure 13 shows the relative error in the Abaqus simulation over the interval $0 \leq x \leq 5$ where the numerical solution accuracy approaches 6 significant digits for $n = 300$ terms in Eq. A-3; with $A_1, ... A_N, B_1, ..., B_N$ constants, $k = N = 6$ in Eq. 26. The relative error is greatest over the interval $0 \leq x \leq 0.5$ and becomes undefined near $x = 0.6$ where the normal stress solution $\sigma_{yy}(0.6, 0.2) \rightarrow 0$ (Eq. 31), and therefore the relative error at this location is undefined. Figure 14 shows the relative error in the Abaqus simulation over the interval $0 \leq x \leq 5$ where the numerical solution accuracy approaches 6 significant digits for $n = 300$ terms in Eq. A-3; with $A_1, ... A_N, B_1, ..., B_N$ constants, $k = N = 6$ in Eq. 26. The relative error is at a minimum over the interval $0 \leq x \leq 2$ and becomes undefined near $x = 2.65$ where the shear stress solution $\sigma_{xy}(2.65, 0.2) \rightarrow 0$ (Eq. 32), and therefore the relative error at this location is undefined. Figures 13 and 14 demonstrate that the XFEM implementation in Abaqus can be used to accurately predict the classical static stress fields in a linear elastic medium with a crack.
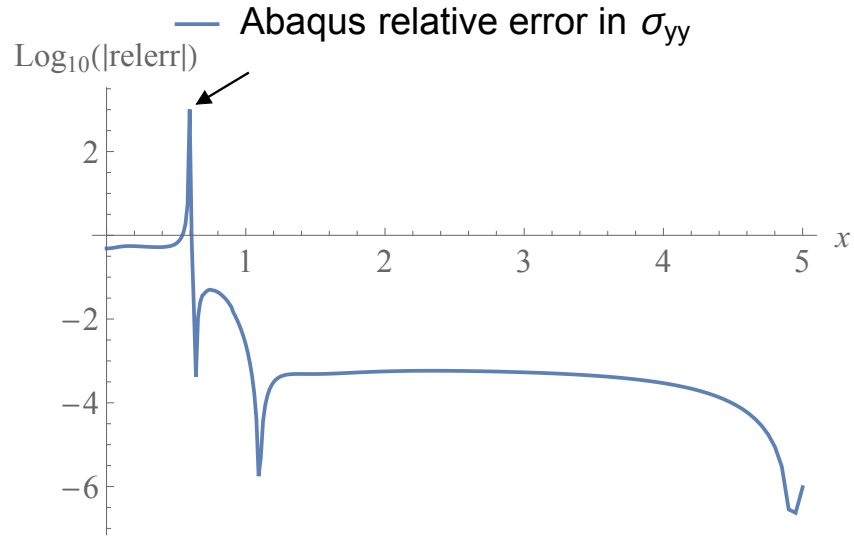
Fig. 13 Relative error of the normal stress determined with Abaqus (refined mesh model of Section 8) vs. Gauss-Chebyshev numerical integration shown in Fig. 5 over the space interval $0 \leq x \leq 5$. The arrow indicates where then normal stress has a zero-crossing $\Sigma(x, h_1) = \sigma_{yy}(x, 0.2) \to 0$ in Fig. 5 and increases the error according to Eq. 35.
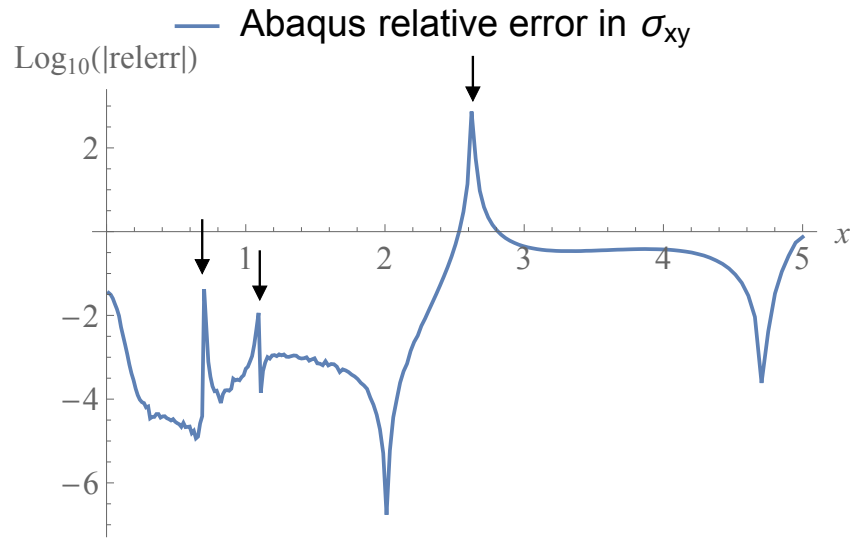
Fig. 14 Relative error of the shear stress determined with Abaqus (refined mesh model of Section 8) vs. Gauss-Chebyshev numerical integration shown in Fig. 6 over the space interval $0 \leq x \leq 5$. The arrows indicate where the shear stress has a zero-crossing $\Sigma(x, h_1) = \sigma_{xy}(x, 0.2) \to 0$ in Fig. 6 and increases the error according to Eq. 35.

8. Abaqus Finite Element Modeling

The computational FE modeling is done with Abaqus/Standard using the XFEM capability. The XFEM enriches elements with added degrees of freedom that allow for the modeling of discontinuities, specifically the discontinuous displacement field across the crack surfaces and the asymptotic crack-tip stress field. SIFs can be calculated from contour integration (J-integrals) around the crack tip. While the XFEM does not require the crack surface or tip be congruent with the mesh, because of how the contour paths for the J-integral are computed, a regular mesh that is relatively aligned (e.g., parallel) to the crack reduces error and is desirable.[35,36]

The numerical solution to the singular integral equations assumes plane strain conditions, but the XFEM, which incorporates asymptotic fields in Abaqus, is only implemented in 3-dimensional (3-D) analyses for stationary cracks. Therefore, boundary conditions have to be applied to the 3-D FE geometry to simulate plane strain conditions. The geometry and boundary conditions are shown in Fig. 15. The geometry uses half-symmetry at $x = 0$ with the x-displacement fixed and the crack parallel to the x-axis. The y-displacements are fixed on the top surface and a tensile distributed load is applied to the bottom surface, similar to Fig. 3(c). To approximate plane strain conditions, the z-direction thickness is small compared the lateral dimensions ($L = 5$, $W = 10$, $T = 1$) and the displacements in the z-direction are fixed on both z-direction faces to restrict the thickness from changing because of the Poisson effect. The mesh is biased in the x- and y-directions so that it is uniform and refined at the crack tip, with the bias allowing larger elements at the edges of the model furthest from the crack tip. It will be shown that while acceptable results for the SIFs can be calculated using a relatively coarse mesh, convergence of the stress state requires a more heavily refined mesh because of the singular nature of the stresses near the crack tip. The models using the coarse mesh have approximately 100,000 elements with an element size around the crack tip of 0.025 and a maximum size of 0.125. The refined mesh model used for the stress comparison has approximately 3.9 million elements with the element size varying between 0.015 and 0.05.
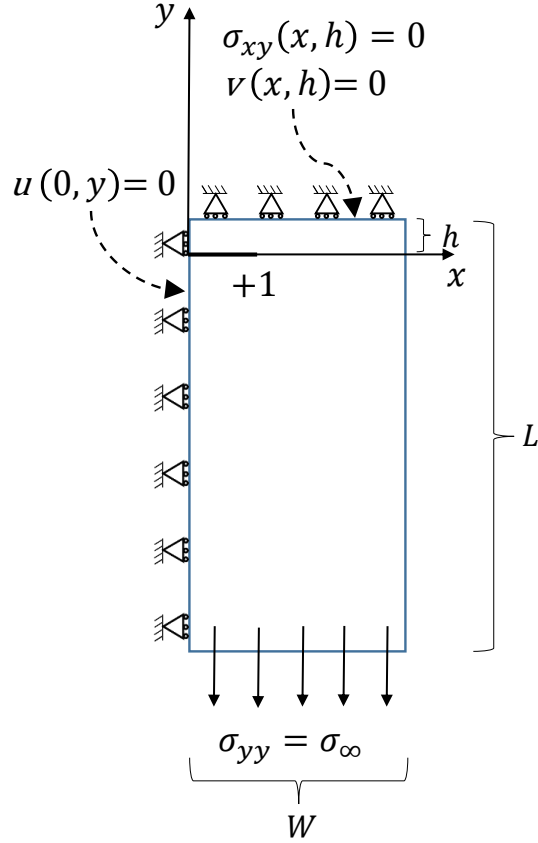
Fig. 15 Schematic of the Abaqus FE model

Abaqus computes the SIFs for a requested number of contours. The SIFs are typically inaccurate for the contours nearest to the crack tip and often oscillates around the correct value.[35,36] For the purposes of this work, the SIFs are calculated for 10 contours, with the values from the 2 contours nearest to the crack tip being omitted due to their inaccuracy, and the remaining 8 contours being averaged for the reported SIF value. For the coarse mesh, the SIF values for $a/h = 1.0, 1.25, 1.\overline{66}$ are shown in Table 2. The refined mesh is used to calculate the SIFs for $a/h = 1.\overline{66}$ using the same averaging procedure, and Table 3 shows the average values compared with both the coarse mesh and the values determined using Eq. 28. Since the coarse mesh produced comparable results to the solution using Eq. 28, the normalized SIFs for $a/h = 1.0, 1.25$ are not calculated for the refined mesh. The mesh refinement does have an effect on the stress field near the crack. The coarse mesh does not produce smooth stress results for comparison to the numerical Gauss-Chebyshev solution, so the stress solution for the refined mesh is used.

Table 2 Normalized SIFs from Abaqus contour integration

| Contour | a/h | | | | | |
| | 1.0 | | 1.25 | | $1.\overline{66}$ | |
	F_I	F_{II}	F_I	F_{II}	F_I	F_{II}
1	1.0454	–0.0208	1.0590	–0.1294	1.1397	–0.2048
2	0.9535	–0.1047	0.9253	–0.1338	0.9247	–0.0816
3	0.8689	–0.0545	0.8316	–0.0919	0.7887	–0.1149
4	0.8801	–0.0742	0.8660	–0.0737	0.8180	–0.1023
5	0.8971	–0.0506	0.8643	–0.0737	0.8141	–0.1036
6	0.8886	–0.0666	0.8604	–0.0786	0.8006	–0.1106
7	0.8672	–0.0588	0.8361	–0.0850	0.8062	–0.1082
8	0.8886	–0.0566	0.8553	–0.0845	0.7983	–0.1126
9	0.8790	–0.0609	0.8497	–0.0761	0.7961	–0.1126
10	0.8762	–0.0576	0.8440	–0.0824	0.7955	–0.0990
Avg (3–10)	0.8807	–0.0600	0.8510	–0.0798	0.8022	–0.1078

Table 3 Comparison of the effect of Abaqus mesh refinement for $a/h = 1.\overline{66}$. The average values for F_I and F_{II} compared with the Eq. 28 values.

| Coarse Mesh | | Refined Mesh | | Numerical values Eq. 28[a] | |
F_I	F_{II}	F_I	F_{II}	F_I	F_{II}
0.8022	–0.1078	0.8100	–0.1098	0.7860	–0.1011

[a] Numerical values are from Table B-1, $N = 9$.

9. Conclusions

In this report, the method of integral transforms[21] and methods developed by Erdogan and Gupta[22,23] were used to solve the problem of a crack parallel to a rigid boundary under remote tension. We derived a system of singular integral equations of the first kind, specific to the problem at hand, which we numerically solved using Gauss-Chebyshev integration. SIFs were calculated for this problem which were in excellent agreement with those derived by others using different solution methods.[25–27]

Expressions for the normal stress $\sigma_{yy}(x, y)$ and shear stress $\sigma_{xy}(x, y)$ fields were derived for the region between the crack and the rigid boundary (shear-stress free symmetry plane). We demonstrated that this region is indeed in a state of compression, as our prior FE simulations indicated[1] and despite the remotely applied tensile prestress. Full-field elastostatic stress solutions to stationary crack problems involving boundaries, such as those derived in this report, are somewhat rare to find in the literature, although such solutions are necessary for verification of FE code simulations involving cracks; most papers of this nature involve calculation and tabulation of only the SIFs.

We specialized our results in Eq. 31 and Eq. 32 to the problem of a crack in an infinite plate under remote tension and showed that the relative error in our numerically derived solutions are within machine precision of the closed-form analytical solutions found in Zehnder.[28] We also demonstrated that both the SIFs and stress fields derived via numerical solution of the singular integral equations, compared well with those determined using the commercially available Abaqus[2] FE code. Using these results, we estimated the relative error between the normal and shear stress distributions using our numerical solution of the singular integral equations and Abaqus FE results; it was found that with a relatively refined FE mesh, Abaqus provided accurate estimates of the normal $\sigma_{yy}(x, y)$ and shear stress $\sigma_{xy}(x, y)$ fields in the vicinity of a stationary crack modeled using the XFEM. Still requiring verification with the XFEM in Abaqus are problems involving elastodynamic fields that impinge upon stationary or dynamically propagating cracks.

10. References

1. Sahane D, Santare MH, Powers BM, Gazonas GA. Computational simulations of wave propagation in microcrack-damaged media under prestress. Int J Fracture. 2016;199:185–198.

2. Abaqus user's manual. Ver. 6.14. Providence (RI): Dassault Systemes Simulia, Inc.; 2013.

3. Biot MA. The influence of initial stress on elastic waves. J Appl Phys. 1940;11(8):522–530.

4. Biot MA. Mechanics of incremental deformations. 3rd ed. New York, (NY): Wiley; 1965.

5. Vermeersen LLA, Vlaar NJ. The gravito-elastodynamics of a pre-stressed elastic earth. Geophys J Intl. 1991;104(3):555–563.

6. Archambeau C, Sammis C. Seismic radiation from explosions in prestressed media and the measurement of tectonic stress in the earth. Rev Geophys and Space Phys. 1970;8(3):473–499.

7. Flavin JN. Thermo-elastic Rayleigh waves in a prestressed medium. Proc Cambridge Philos Soc. 1962;58(3):532–538.

8. Norris AN, Sinha BK. The speed of a wave along a fluid/solid interface in the presence of anisotropy and prestress. J Acous Soc Am. 1995;98(2):1147–1154.

9. Liu QH, Sinha BK. A 3D cylindrical PML/FDTD method for elastic waves in fluid-filled pressurized boreholes in triaxially stressed formations. Geophysics. 2003;68(5):1731–1743.

10. Cardamone L, Valentin A, Eberth JF, Humphrey JD. Origin of axial prestretch and residual stress in arteries. Biomech Model Mechanobiol. 2009;8(6):431–446.

11. Gei M, Colonnelli S, Springhetti R. The role of electrostriction on the stability of dielectric elastomer actuators. Int J Solids Struct. 2014;51(3–4):848–860.

12. Danas K, Kankanala SV, Triantafyllidis N. Experiments and modeling of iron-particle-filled magnetorheological elastomers. J Mech Phys Solids. 2012;60(1):120–138.

13. Rabczuk T, Eibl J. Numerical analysis of prestressed concrete beams using a coupled element free Galerkin/finite element approach. Int J Solids Struct. 2004;41(3–4):1061–1080.

14. Holmquist TJ, Johnson GR. Modeling prestressed ceramic and its effect on ballistic performance. Int J Impact Eng. 2005;31(2):113–127.

15. Jeon B, Stewart RJ, Ahmed IZ. Peridynamic simulations of brittle structures with thermal residual deformation: strengthening and structural reactivity of glasses under impacts. Proc R Soc Lond A. 2015;471(2183):20150231.

16. Su D, Santare MH, Gazonas GA. The effect of crack face contact on the anisotropic effective moduli of microcrack damaged media. Eng Fract Mech. 2007;74(9):1436–1455.

17. Su D, Santare MH, Gazonas GA. An effective medium model for elastic waves in microcrack damaged media. Eng Fract Mech. 2008;75(14):4104–4116.

18. Wang X, Santare MH, Gazonas GA. Anisotropic effective moduli of microcracked materials under antiplane loading. Eng Fract Mech. 2009;76(12):1910–1919.

19. Wang X, Gazonas GA, Santare MH. On the effective electroelastic properties of microcracked generally anisotropic solids. Int J Fracture. 2009;158(1):27–40.

20. Souza FV, Allen DH. Modeling the transition of microcracks into macrocracks in heterogeneous viscoelastic media using a two-way coupled multiscale model. Int J Solids Struct. 2011;48(22–23):3160–3175.

21. Sneddon IN. The use of integral transforms. New York, (NY): McGraw-Hill; 1972.

22. Erdogan F, Gupta GD. The stress analysis of multi-layered composites with a flaw. Int J Solids Struct. 1971;7(1):39–61.

23. Erdogan F, Gupta GD, Cook TS. Numerical solution of singular integral equations. In: Sih GC, editor. Mechanics of Fracture I: Methods of Analysis and Solutions of Crack Problems; Netherlands (Leyden): Noordhoff International Publishing; 1973. p. 368–425.

24. Kantorovich LV, Krylov VI. Approximate methods of higher analysis. New York (NY): Interscience; 1964.

25. Chang CY, Ma CC. The mixed-mode fracture analysis of multiple embedded cracks in a semi-infinite plane by an analytical alternating method. J Press Vessel Technol. 2002;124(4):446–456.

26. Yokobori T, Uozumi M, Ichikawa M. Interaction between overlapping parallel elastic cracks. J Jpn Soc Strength Fract Mater. 1971;6:39–50.

27. Kamei A, Yokobori T. Some results on the stress intensity factors of cracks and/or slip bands systems. Tohoku (Japan): Tohoku University; 1974. Reports of the Research Institute for Strength and Fracture of Materials No.: 10.

28. Zehnder AT. Fracture mechanics. Pfeiffer F, Wriggers P, editors. New York (NY): Springer; 2012. (Lecture Notes in Applied and Computational Mechanics; vol. 62).

29. Titchmarsh EC. Introduction to the theory of Fourier integrals. 2nd ed. Oxford (UK): Clarendon Press; 1948.

30. Erdogan F. Stress intensity factors. Trans Am Soc Mech Eng. 1973;50:992–1002.

31. Erdogan F. Bonded dissimilar materials containing cracks parallel to the interface. Eng Fract Mech. 1971;3:231–240.

32. Abramowitz M, Stegun I. Handbook of mathematical functions. 9th ed. New York (NY): Dover Publications; 1970.

33. Mathematica edition Ver. 10.0. Champaign (IL): Wolfram Research; 2013.

34. Oberkampf WL, Roy CJ. Verification and validation in scientific computing. Cambridge (UK): Cambridge University Press; 2010.

35. Leven M, Rickert D. Stationary 3D crack analysis with Abaqus XFEM for integrity assessment of subsea equipment [master's thesis]. [Göteberg (Sweden)]: Chalmers Institute of Technology; 2012.

36. McNary MJ. Implementation of the Extended Finite Element Method (XFEM) in the ABAQUS Software Package [master's thesis]. [Atlanta (GA)]: Georgia Institue of Technology; 2009.

INTENTIONALLY LEFT BLANK.

Appendix A. Coefficient Definitions for Equation 27

In this appendix, we provide the additional equations needed to numerically evaluate the constants A_k and B_k from Eq. 27. On substituting these constants into the definite integrals in Eq. 10 and Eq. 12, the stresses and displacements anywhere in the domain can be determined (cf. Section 5 where we calculate the normal stresses $\sigma_{yy}(x, y)$, and shear stresses $\sigma_{xy}(x, y)$ in the finite strip between the crack line $y = 0$ and rigid boundary $y = h$ and compare our results with computational finite element results using Abaqus).

The definitions of constants a_{kn}, b_{kn}, c_{kn}, and d_{kn} that appear in Eq. 27 can be found on page 394 of Erdogan et al.[1] are given as

$$a_{kn} = \int_{-1}^{1} U_{2k-1}(x) H_n^{11}(x) \sqrt{1 - x^2} \, dx \, ,$$

$$b_{kn} = \int_{-1}^{1} U_{2k-1}(x) H_n^{12}(x) \sqrt{1 - x^2} \, dx \, ,$$

$$\text{(A-1)}$$

$$c_{kn} = \int_{-1}^{1} U_{2k-2}(x) H_n^{21}(x) \sqrt{1 - x^2} \, dx \, ,$$

$$d_{kn} = \int_{-1}^{1} U_{2k-2}(x) H_n^{22}(x) \sqrt{1 - x^2} \, dx \, ,$$

where $U_{2k-1}(x)$ and $U_{2k-2}(x)$ are Chebyshev polynomials of the second kind, and

---

[1] Erdogan F, Gupta GD, Cook TS. Numerical solution of singular integral equations. In: Sih GC, editor. Mechanics of Fracture I: Methods of Analysis and Solutions of Crack Problems; Netherlands (Leyden): Noordhoff International Publishing; 1973. p. 368–425.

polynomial functions $H_n^{ij}(x)$ are defined on page 393 of Erdogan et al.[1] as

$$H_n^{11}(x) = \frac{1}{\pi} \int_{-1}^{1} k_{11}(x,t) T_{2n}(t) \left(1 - t^2\right)^{-\frac{1}{2}} dt \,,$$

$$H_n^{12}(x) = \frac{1}{\pi} \int_{-1}^{1} k_{12}(x,t) T_{2n-1}(t) \left(1 - t^2\right)^{-\frac{1}{2}} dt \,,$$

$$\text{(A-2)}$$

$$H_n^{21}(x) = \frac{1}{\pi} \int_{-1}^{1} k_{21}(x,t) T_{2n}(t) \left(1 - t^2\right)^{-\frac{1}{2}} dt \,,$$

$$H_n^{22}(x) = \frac{1}{\pi} \int_{-1}^{1} k_{22}(x,t) T_{2n-1}(t) \left(1 - t^2\right)^{-\frac{1}{2}} dt \,,$$

where $T_{2n}(x)$ and $T_{2n-1}(x)$ are Chebyshev polynomials of the first kind, and the kernel functions $k_{ij}(x,t)$ in Eq. A-2 are given in Eq. 25. In practice, polynomial functions $H_n^{ij}(x)$ in Eq. A-2 are determined in Mathematica[2] using Gauss-Chebyshev numerical integration with $n = 300$ terms,[3] viz.,

$$\int_{-1}^{1} \frac{f(x,t)}{\sqrt{1 - t^2}} dt \approx \sum_{i=1}^{n} w_i f(x, t_i) \quad , \tag{A-3}$$

with weights, $w_i = \frac{\pi}{n}$ and abscissas, $t_i = \cos(\frac{(2i-1)\pi}{(2n)})$ obtained from the zeros of the orthogonal Chebyshev polynomials of the first kind (cf. Eq. 25.4.38 on page 889 of Abramovitz and Stegun[4]).

The polynomial functions $H_n^{ij}(x)$ determined with Eq. A-3 are then substituted into Eq. A-1 for determining constants a_{kn}, b_{kn}, c_{kn}, and d_{kn} used in system Eq. 27. Gauss-Chebyshev numerical integration with $n = 300$ terms, is again employed

---

[2] Mathematica edition Ver. 10.0. Champaign (IL): Wolfram Research; 2013.

[3] Numerical integration using $n = 300$ terms brings the numerical solution accuracy to 15 significant digits which is at machine precision, cf. Fig. 10.

[4] Abramowitz M, Stegun I. Handbook of mathematical functions. 9th ed. New York (NY): Dover Publications; 1970.

using Mathematica[2] to solve Eq. A-1 with approximation,

$$\int_{-1}^{1} f(x,t)\sqrt{1-t^2}\,dt \approx \sum_{i=1}^{n} w_i f(x,t_i) \quad , \tag{A-4}$$

with weights, $w_i = \frac{\pi}{n+1}\sin^2\left(\frac{i\pi}{n+1}\right)$ and abscissas, $t_i = \cos\left(\frac{i\pi}{n+1}\right)$ obtained from the zeros of the orthogonal Chebyshev polynomials of the second kind (cf. Eq. 25.4.40 on page 889 of Abramovitz and Stegun (1970)[4]).

As an example, for $N = 3$ system Eq. 27 appears in matrix-vector form as,

$$a\,\vec{x} = \vec{b} \quad , \tag{A-5}$$

where,

$$a = \begin{bmatrix} \frac{\pi}{2} + a_{11} & a_{12} & a_{13} & b_{11} & b_{12} & b_{13} \\ a_{21} & \frac{\pi}{2} + a_{22} & a_{23} & b_{21} & b_{22} & b_{23} \\ a_{31} & a_{32} & \frac{\pi}{2} + a_{33} & b_{31} & b_{32} & b_{33} \\ c_{11} & c_{12} & c_{13} & \frac{\pi}{2} + d_{11} & d_{12} & d_{13} \\ c_{21} & c_{22} & c_{23} & d_{21} & \frac{\pi}{2} + d_{22} & d_{23} \\ c_{31} & c_{32} & c_{33} & d_{31} & d_{32} & \frac{\pi}{2} + d_{33} \end{bmatrix} \tag{A-6}$$

$$\vec{x} = \begin{bmatrix} A_1 \\ A_2 \\ A_3 \\ B_1 \\ B_2 \\ B_3 \end{bmatrix} \quad , \quad \vec{b} = \begin{bmatrix} 0 \\ 0 \\ 0 \\ -\frac{\pi}{2}\,P_0\,\frac{\kappa+1}{2\mu} \\ 0 \\ 0 \end{bmatrix} \quad . \tag{A-7}$$

The vector $\vec{x}$ or the constants $A_1, A_2, A_3, B_1, B_2, B_3$ for $N = 3$ are obtained by finding the inverse of non-symmetric constant matrix a given by Eq. A-6, and post-multiplying this by $\vec{b}$ defined by F_{1k} and F_{2k} in Eq. 27, i.e., $\vec{x} = a^{-1}\vec{b}$. Given the $A_1, A_2, A_3, B_1, B_2, B_3$ enables determination of approximate values for the dislocation densities in Eq. 26, which together with $A_{ij}(\xi)$ in Eq. 18 enables determination of the displacement and stresses throughout the medium. In addition, the calculation of stress intensity factors (SIFs) is rather straightforward and discussed in Section 4. Table B-1 in Appendix B illustrates SIF convergence for $N = 3, 6, 9$.

INTENTIONALLY LEFT BLANK.

Appendix B. Stress Intensity Factor Convergence

Table B-1 Normalized SIFs for 2 parallel cracks in an infinite plane under remote tension, where $K_I = F_I \sigma \sqrt{\pi a}$, $K_{II} = F_{II} \sigma \sqrt{\pi a}$, and $k_1 = F_I$; $k_2 = F_{II}$ are determined using Eq. 28

a/h	F_I ($N = 3$)	F_I ($N = 6$)	F_I ($N = 9$)	F_{II} ($N = 3$)	F_{II} ($N = 6$)	F_{II} ($N = 9$)
0.01	0.99996	0.99996	0.99996	-1.8747×10^{-7}	-1.8747×10^{-7}	-1.8747×10^{-7}
0.1	0.9963	0.9963	0.9963	–0.00018	–0.00018	–0.00018
0.2	0.9857	0.9857	0.9857	–0.0014	–0.0014	–0.0014
0.4	0.9505	0.9505	0.9505	–0.0094	–0.0094	–0.0094
0.6	0.9086	0.9086	0.9086	–0.0246	–0.0246	–0.0246
0.8	0.8706	0.8707	0.8707	–0.0429	–0.0429	–0.0429
1.0	0.8403	0.8404	0.8404	–0.0607	–0.0607	–0.0607
1.25	0.8130	0.8131	0.8131	–0.0793	–0.0793	–0.0793
$1.\overline{66}$	0.7864	0.7860	0.7860	–0.1008	–0.1011	–0.1011
2.0	0.7754	0.7737	0.7737	–0.1122	–0.1128	–0.1128
5.0	0.7504	0.7441	0.7445	–0.1649	–0.1566	–0.1567
10.0	0.6941	0.7441	0.7385	–0.1992	–0.1785	–0.1792

1   DEFENSE TECHNICAL
(PDF)   INFORMATION CTR
         DTIC OCA

2   DIRECTOR
(PDF)   US ARMY RESEARCH LAB
         RDRL CIO L
         IMAL HRA MAIL & RECORDS MGMT

1   GOVT PRINTG OFC
(PDF)   A MALHOTRA